Solar Energy Materials & Solar Cells 301 (2026) 114284

Contents lists available at ScienceDirect

Solar Energy Materials and Solar Cells

journal homepage: www.elsevier.com/locate/solmat

$CuInSe_2$-based micro-concentrator solar cells fabricated from In islands grown by laser-assisted MO-CVD

J. Berger [a,*], S. Zahedi-Azad [b], H. Voss [c], O.C. Ernst [b,d], R. Hammerschmidt [e], T. Boeck [b], J. Martin [b], J. Bonse [c], J. Krüger [c], M. Schmid [a]

[a] Fakultät für Physik und CENIDE, Universität Duisburg-Essen (UDE), Forsthausweg 2, 47057, Duisburg, Germany
[b] Leibniz-Institut für Kristallzüchtung (IKZ), Max-Born-Str. 2, 12489, Berlin, Germany
[c] Bundesanstalt für Materialforschung und -prüfung (BAM), Unter Den Eichen 87, 12205, Berlin, Germany
[d] Brandenburg University of Technology Cottbus-Senftenberg (BTU), Universitätsplatz 1, 01968, Senftenberg, Germany
[e] Bestec GmbH, Am Studio 2b, 12489, Berlin, Germany

A B S T R A C T

Micro-concentrator solar cells offer a promising route for reducing material usage in photovoltaics. For $Cu(In,Ga)Se_2$, multiple micro-concentrator manufacturing methods have already been evaluated. All of them involve either high preparation complexity or post-processing to recycle unused precursor or absorber materials. In this work, a new method using laser-assisted metal-organic chemical vapor deposition (LA-MOCVD) was applied to directly grow arrays of indium micro-islands. These arrays are examined and further processed to $CuInSe_2$ micro-solar cell arrays. The geometry and morphology of the islands were investigated and compared before and after absorber formation. The investigation shows that the absorber growth is limited to the vertical direction normal to the substrate surface and that the starting morphology is preserved. Furthermore, the absorber island arrays are processed into micro-modules and operational solar cells are achieved as a proof of principle. These not yet optimized arrays reach a conversion efficiency of 0.65% under 1 sun illumination. Under 17 suns of light concentration, the efficiency gain is between 60 and 250%. This work demonstrates the method's viability for the fabrication of micro-solar cell arrays, with clear potential for achieving higher conversion efficiencies through future optimization.

1. Introduction

Renewable energies have become increasingly important in our modern society for addressing climate change and achieving the global objective of limiting temperature rise to below 2 °C, as outlined in the Paris Agreement. In this context, efficient use of resources is paramount. In chalcopyrite solar cells and many other photovoltaic (PV) technologies, this can be achieved by reducing the layer thickness. In $Cu(In,Ga)Se_2$ (CIGSe) solar cells, the absorber thickness can be reduced from 2 µm down to 500 nm, effectively cutting down the material consumption by a factor of 4. Another option is to reduce the cells' lateral area and use light concentration onto the reduced area to boost efficiency [1]. This concept is applied in micro-concentrator solar cells, where arrays of micrometer-sized solar cells in the range of 50–500 µm diameter and a pitch of up to a few millimeters are combined with concentrator optics, resulting in concentration factors from around 10 up to 40,000 suns. In order to save material, the cells need to be directly grown in their final size in a bottom-up approach [2–5] or excess material needs to be recycled [6]. The miniaturization also has benefits in heat dissipation, reducing the need for active cooling under light concentration [7,8].

For CIGSe, a proof of concept for micro-concentrator solar cells was already demonstrated in a top-down manner, promising up to 5% efficiency gain under 475 suns concentration [9–11]. The top-down approach was done either by shading, etching (laser, chemical) or scribing. Additionally, loss mechanisms were analyzed [9]. Alternatively, multiple bottom-up approaches were investigated [2–5,8,12,13]. One promising method uses a photoresist mask and electrodeposition to grow the precursor into the lithography pattern [5,8]. Another method is laser patterning the substrate to provide nucleation sites for indium deposition. With the right deposition temperature and a distance between the patterned spots corresponding to the mean free path on the surface, indium will nucleate locally and material is saved [2,4,12,13]. For the electrodeposition and the PVD-based direct growth, the substrate needs to be prepared or patterned. A third method is the deposition of a planar precursor onto a transfer substrate and using a femtosecond laser to transfer the precursor via laser-induced forward transfer (LIFT) as islands onto a new sample [3,12]. After deposition of the precursor layers, a selenization step for all the methods is necessary.

* Corresponding author.
E-mail address: jan.lucassen@uni-due.de (J. Berger).

https://doi.org/10.1016/j.solmat.2026.114284
Received 17 December 2025; Received in revised form 24 February 2026; Accepted 6 March 2026
Available online 13 March 2026

While promising, these approaches generally require pre- or post-processing.

In this work, we manufacture and investigate arrays of indium islands and subsequent $CuInSe_2$ (CISe) absorbers on molybdenum films. The indium arrays are obtained with laser-assisted metal-organic chemical vapor deposition (LA-MOCVD) [14], a method for localized growth of metal precursors from metal-organic vapor. LA-MOCVD has the advantage that nucleation happens directly at the illuminated spots, where the additionally required heat is supplied to the preheated substrate. There is no physical restriction in diameter and especially in pitch, compared to growing on a patterned substrate. The island size depends on the used lens array or diffractive optical element (DOE). Moreover, there are no pre-processing steps. A lens array could be used to deposit precursor material with exactly the geometry of the array's focal distribution. The same array geometry could later be applied for light concentration, thus allowing for ideal alignment. Other advantages of the LA-MOCVD approach are the possibility of depositing other materials, e.g. gallium and copper, sequentially or, depending on their cracking temperature, simultaneously. The method promises an easily scalable process capable of adjusting the pitch and diameter of the indium spots. In this paper, these indium arrays are morphologically investigated and then further processed to CISe absorbers and solar cells, testing the capability of the process for production of bottom-up grown micro-concentrator solar cells.

2. Experimental section/methods

2.1. Substrate

All samples were deposited on 3-mm-thick soda-lime glass substrates with 800 nm of molybdenum sputtered on top.

2.2. Laser-assisted MO-CVD

For the laser-assisted MOCVD (LA-MOCVD), a custom-designed cluster system was built and installed at IKZ (Leibniz-Institut für Kristallzüchtung, Berlin, Germany) by Bestec GmbH, Berlin, Germany. The laser system used for the laser heating is a 10 W continuous-wave (cw) laser with 1070 nm wavelength from Dr. Mergenthaler GmbH & Co. KG, Neu-Ulm, Germany.

The main chamber of the cluster is the LA-MOCVD, capable of depositing indium via decomposition of trimethylindium ($In(CH_3)_3$). During deposition, the Mo-coated substrate was first radiatively heated to a temperature of 350–380 °C inside the main chamber. An array of 7 × 7 focused laser spots, generated by passing the cw laser beam through a Diffractive Optical Element (DOE), was then directed onto the substrate. The DOE was custom-designed and fabricated by the Fraunhofer Institute for Telecommunications, Heinrich-Hertz-Institut (HHI), Berlin, Germany. It consists of a binary phase mask reactive ion etched in fused silica. It was designed to create an array of 7 × 7 Gaussian spots with a pitch of 750 μm from an input laser beam of 5 mm diameter. At each spot (43.5 ± 5 μm radius), the surface temperature is locally increased by approximately 80 °C at the spot center according to Ref. [14]. This brought the final temperature well above the cracking temperature of 340 °C for the $In(CH_3)_3$ precursor, starting efficient localized indium deposition. The decomposition is a gradual process starting at 340 °C and reaching nearly 100 % decomposition rate at 420 °C [15]. The temperature profile on the substrate has a larger full-width at half-maximum than the initial laser spot due to thermal diffusion, in particular caused by the heat conductivity of the molybdenum layer [14]. The size and pitch of the absorber islands are chosen for a concentration factor of 447 suns, which is close to the best concentration factor found by Paire et al. [11] and allows concentrated illumination without active cooling [7]. Moreover, the size of an individual In-island is also chosen to ensure sufficient copper and selenium diffusion during further processing [4]. All samples used in this paper were produced at 350 °C initial substrate temperature, 180 s irradiation at 5.2 W total laser output power and 20 mbar pressure. The carrier gas was nitrogen at 1000 sccm flow rate while the $In(CH_3)_3$ flow rate was set to 100 sccm.

2.3. Characterization methods

The scanning electron microscope (SEM) used for imaging in this work was an FEI Inspect F operated at an electron acceleration voltage of 30 kV in ETD(SE) mode. A Dektak Line Profilometer was used for recording the height profiles. All arrays were characterized following the initial indium deposition and again after their conversion to absorbers. For the micro-Raman measurements in backscattering geometry, a 532-nm-wavelength diode laser with 50 mW power, 0.81 μm spot size, and a Kymera grating spectrograph from Oxford Instruments, paired with a CCD camera from Andor Technology with 1600 × 200 pixels of 16 μm × 16 μm size and a resulting spectral resolution of 0.05 to 0.07 nm, were used. The acquisition time was 90 s. The grating had 1800 lines/mm. For the current-voltage (IV) measurements, two solar simulators were applied: the first one was calibrated to 1-sun illumination (AM1.5G), and the second one was a concentrator type calibrated to reach from 0.5 to around 17 suns with the use of filters and a Fresnel lens. Both solar simulators are utilizing a Peltier-cooled plate ensuring 25 °C sample temperature for standard test conditions. The IV-T measurement was performed in a closed-cycle helium cryostat. First, the sample was cooled to approximately 160 K and then measured in ~10 K steps up to 300 K. For the measurement, the cryostat was placed underneath the concentrator type solar simulator, yet set to 1 sun intensity.

2.4. Indium array and further processing

Fig. 1 a) displays a schematic of the samples with the positioning of the two arrays A and B per substrate. Array A is closer to the edge and is on the left side. Fig. 1 b) illustrates a schematic of one array. The size of the individual spots varies: the diameter is smallest in the corners and progressively increases towards the center of the array. Each spot is assigned a distinct number to identify its position on the sample. Individual spots within each array are identified by a row-column coordinate system, starting from the top left (position 11). For simplicity in referring to the main diagonal, spots at positions 11, 22, 33, etc., are also referred to by the single digits 1, 2, 3, etc., respectively. Each array is then analyzed using scanning electron microscopy (SEM) and a line profilometer. Fig. 1 c) depicts the intensity pattern of the laser spot array recorded with a fluorescence card mounted in the sample position. It confirms the desired irradiation geometry of the infrared laser beam of 7 × 7 spots with 750 μm spacing and equally reveals a higher intensity moving to the inner spots. The center-to-center distance between the outermost spots is 4.5 mm.

The indium arrays were coated by electron-beam evaporation with a copper film of 500–800 nm thickness, to reach a copper-to-indium ratio of 0.95. Subsequently, the samples were selenized in a rapid thermal processing (RTP) step, at up to 650 °C. The RTP-oven has three zones set to ambient, 350 °C and 700 °C with 800 mbar nitrogen atmosphere. The graphite boat was pushed from zone 1 to zone 2, remaining there for 10 min in order to melt the selenium and alloy the precursor materials. Then it was moved to zone 3 for 6 min, reaching a maximum temperature of 650 °C. Finally, the boat was moved back to zone 2 for 5 min and then to zone 1 to fully cool down to ambient temperature before opening the chamber. The RTP process used 0.005 g of elemental selenium for two 1 × 1-inch substrates with two arrays each. The resulting absorbers were then etched with KCN for 60 s to remove copper selenides. If too much selenium was supplied in the RTP process, the absorbers would peel off due to the molybdenum being fully converted to $MoSe_2$. After etching, all arrays were analyzed again in the SEM and the line profilometer.

The samples were spin-coated with AZ1518 positive photoresist at 6000 rpm for 90 s, followed by a dry bake at 100 °C for 120 s. A 7 × 7

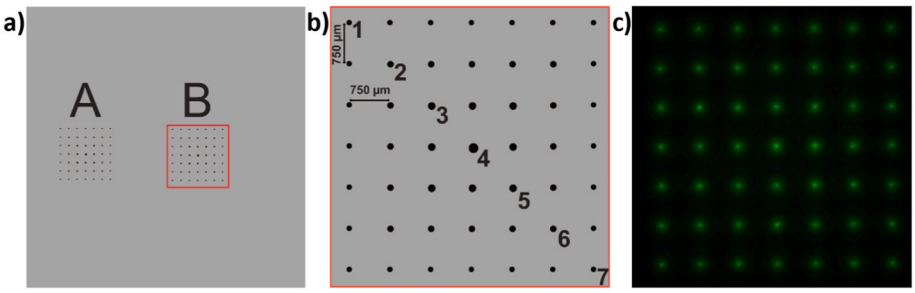

Fig. 1. a): Schematic of the sample layout, showing the two 7 × 7 arrays of micro-islands, designated A and B. b): Schematic of the array. The islands are arranged with a fixed pitch of 750 µm and are identified by a two-digit row-column coordinate. For simplicity, islands along the main diagonal are also referred to by a single-digit number (e.g., position 11 is referred to as 1, 22 as 2, etc.). c): Irradiation pattern of the laser shining through the DOE.

array of absorbers was uncovered by direct-write lithography using a pulsed, 343 nm wavelength, third-harmonic femtosecond laser with 0.05 mW peak power. The direct-write lithography was used to individually adjust the diameter of the openings depending on the diameter in the SEM picture. The openings were chosen to be smaller than the diameter to prevent shunting. After the development of the photoresist, CdS was coated via chemical bath deposition at 80 °C for 6 min. The i-ZnO and AZO window layers were sputtered on top. For electrical measurements, arrays A and B were separated manually, and each array was measured as a single micro-module with 49 micro-cells connected in parallel. On some arrays, a metal grid of Al/Ni was deposited, but it yielded no positive effect. A schematic of the complete cell stack (without the grid) can be seen in Fig. 2 a). In Fig. 2 b) a SEM cross section with EDX of one cell is shown.

As indicated by the color coordination between Fig. 2 a) and 2 b), EDX spectroscopy verifies the Mo and the CISe absorber positions. Elemental profiling reveals a gradient in the Cu:In ratio (ranging from 1.0 to 1.5), while the Cu:Se stoichiometry remains near-constant at 0.5. Some voids are visible in the absorber layer.

3. Results

3.1. Structural characterization

Fig. 3 a) shows an SEM image of the inner 3 × 3 array of indium islands; the islands are clearly separated with no debris visible in between. The innermost islands are the largest, decreasing in size towards the outer edges of the array. Fig. 3 b) depicts the center island (position 4). The island is composed of small, mostly close-packed indium droplets, with some voids visible. At the edges of the island, the droplets become loosely scattered, and the edges are less defined. This change can be clearly seen in Fig. 3 c), which presents the center island at a 60° tilt angle. An outer ring of approx. 20 µm width is much lower and smaller in droplet size than the center, where an increase in droplet size can be seen.

Fig. 3 d) and 3 e) display the same spot after processing to a CISe absorber and after KCN etching (i.e., after removing copper selenide residues). The space between the islands is now filled with small absorber grains, as well as some larger grains. The small grains appear to result from a previously invisible wetting layer of indium [16] rather than from the movement of indium during selenization. Larger debris, as seen in the picture, could result from foreign particles or small corner islands that were not attached properly and seem to be missing in some of the height measurements. The absorbers retain their shape, and distinct features from the indium islands can be directly found in the absorber islands. The change of size towards the edge of the island is seen more clearly in Fig. 3 e). Fig. 3 f) shows the absorber island under the same 60° angle. The formed grains in the center are the largest and shrink towards the outside. However, the height differences cannot be seen due to the low contrast between the absorber grains.

The final absorber morphology is best described as an agglomerate of grains rather than a dense, compact island, a characteristic with significant implications for device performance.

The absorber island in position 4 confirms that most features of the indium island were preserved. The larger droplets and slits are still visible near the center and in the upper half of the island. For direct comparison, an image with markers is provided in the supplementary information (Fig. S1). This observation supports the existence of a wetting layer because no visible migration of indium was observed. Even the features like lined-up droplets at the very edge of the island remained largely in their original positions. Moreover, the small grains are not just around the absorber arrays but cover the entire sample,

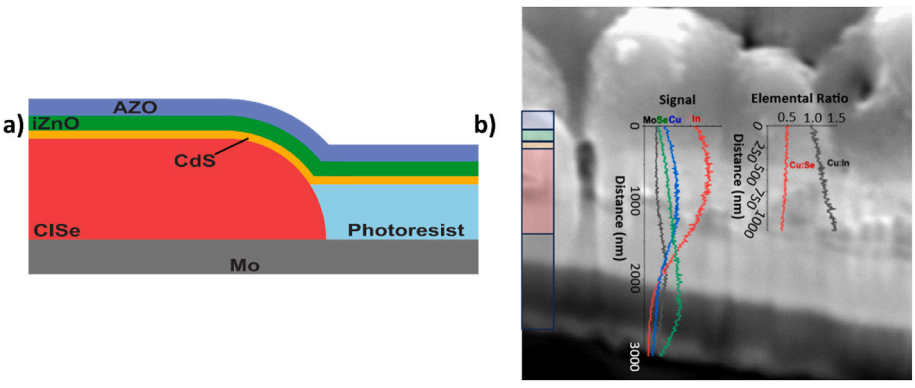

Fig. 2. a) Excerpt from cross-sectional schematic of a single $CuInSe_2$ (CISe) micro-solar cell within the array. The complete device stack consists of the Mo back contact, the CISe absorber, a CdS buffer layer, and the i-ZnO/AZO window layers. b) SEM cross section under 20° angle cut with a focused ion beam with an EDX linescan and the elemental ratio. The colors on the left represent the different layers shown in a). (For interpretation of the references to color in this figure legend, the reader is referred to the Web version of this article.)

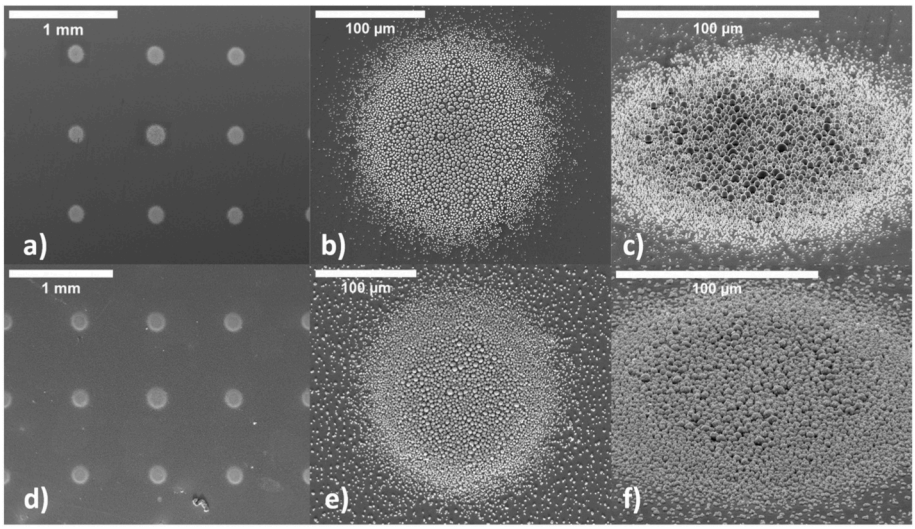

Fig. 3. SEM micrographs comparing the morphology of the indium precursor islands (a-c) with the final CISe absorbers after selenization (d-f). The central 3 × 3 region of the array is shown in (a, d), while close-ups of the central island (center DOE spot) are provided in top-down (b, e) and 60° tilted views (c, f).

which further supports the wetting layer hypothesis [16]. The holes in the center island visible in Fig. 3 b) were closed after selenization, but the boundaries between individual grains at those positions are clearly visible as voids or grain boundaries in the SEM image.

To identify the crystalline phases present, micro-Raman spectroscopy was performed. According to literature, the CISe crystal peak is found around 175 cm^{-1}. Depending on crystal stress, a peak shift for CISe between 173 and 175 cm^{-1} is possible [17]. The peak for $MoSe_2$ is located at 242–245 cm^{-1} [18,19] and copper selenides have peaks around 263 cm^{-1} [20].

In Fig. 4 a), four Raman spectra for different measurement positions and conditions are depicted (vertically shifted for better visibility). The bottom spectrum is a measurement on the back contact prior to KCN etching (pre-KCN etched), showing a relatively weak signal for the absorber as well as for $MoSe_2$. The presence of Cu_2Se or other residues likely scatters and attenuates a significant part of the signal. The three subsequent measurements were performed after etching with KCN. On the etched back contact, the signal for $MoSe_2$ becomes dominant, and across the sample, a small absorber peak appears. When analyzing one of the particles in between the arrays, most of the $MoSe_2$ signal disappears, and only a small peak for the absorber is visible, which is slightly larger than on the pre-KCN back contact. Importantly, the spectrum taken from the center of an absorber island is dominated by the CISe peak, with complete absence of a detectable $MoSe_2$ signal. This confirms that the absorber layer is sufficiently thick and continuous to attenuate the signal from the underlying back contact, a key requirement for fabricating high-quality devices. In Fig. 4 b) all positions are shown in a sketch for better understanding of the measurement.

A key finding is the highly anisotropic nature of the growth during selenization, where the islands grow primarily in height rather than in diameter. In Fig. 5 a), line profilometer scans of the 4th row of the indium array and the absorber array are compared. Taking the copper layer into account, the absorber layer thickness is approximately 1.67 times the thickness of the initial indium-plus-copper stack. However, the pitch between the islands, and in particular their widths remain the same. With a thickness of 1.9 ± 0.17 µm averaged over the measured row for the indium islands and an evaporated copper thickness of 800 nm, the resulting average absorber line thickness is 4.8 ± 0.14 µm.

In Fig. 5 b), the thickness distribution for one full indium array is illustrated, along with the full width at half maximum (FWHM). The size of the bubbles correlates with the FWHM, while the color indicates the height. The diameter of the bubbles was scaled by a factor of two for better visibility, while their centers are at the exact, unscaled real distance. The largest island in diameter and height is at position 4 in the middle. However, the center 3 × 3 islands are all similar. The FWHM evenly reduces towards the edges of the array. The average height over the array is 1.8 ± 0.18 µm, while the FWHM is 79.8 ± 11.26 µm.

Fig. 5 c) presents the absorber island array. The distribution is the

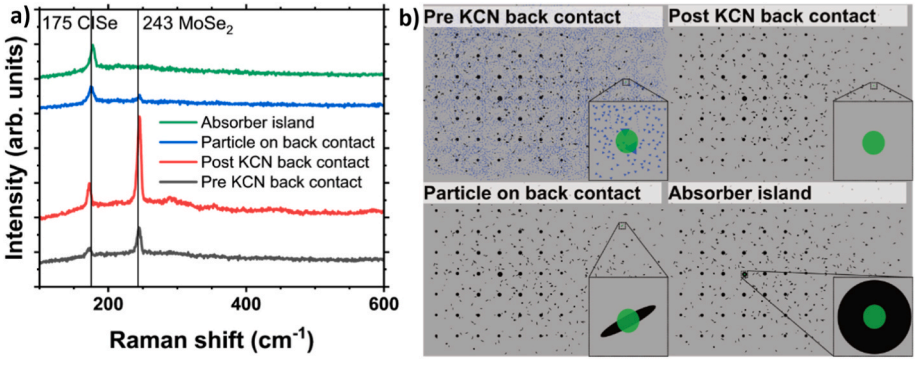

Fig. 4. a) Representative micro-Raman spectra comparing different surface locations before and after KCN etching. The spectra correspond to the CISe absorber island (green), a particle between the islands (blue), and the $MoSe_2$-covered back contact (red; all three after etching), and the unetched back contact (black). b) Sketch of the different measurement positions shown in a). (For interpretation of the references to color in this figure legend, the reader is referred to the Web version of this article.)

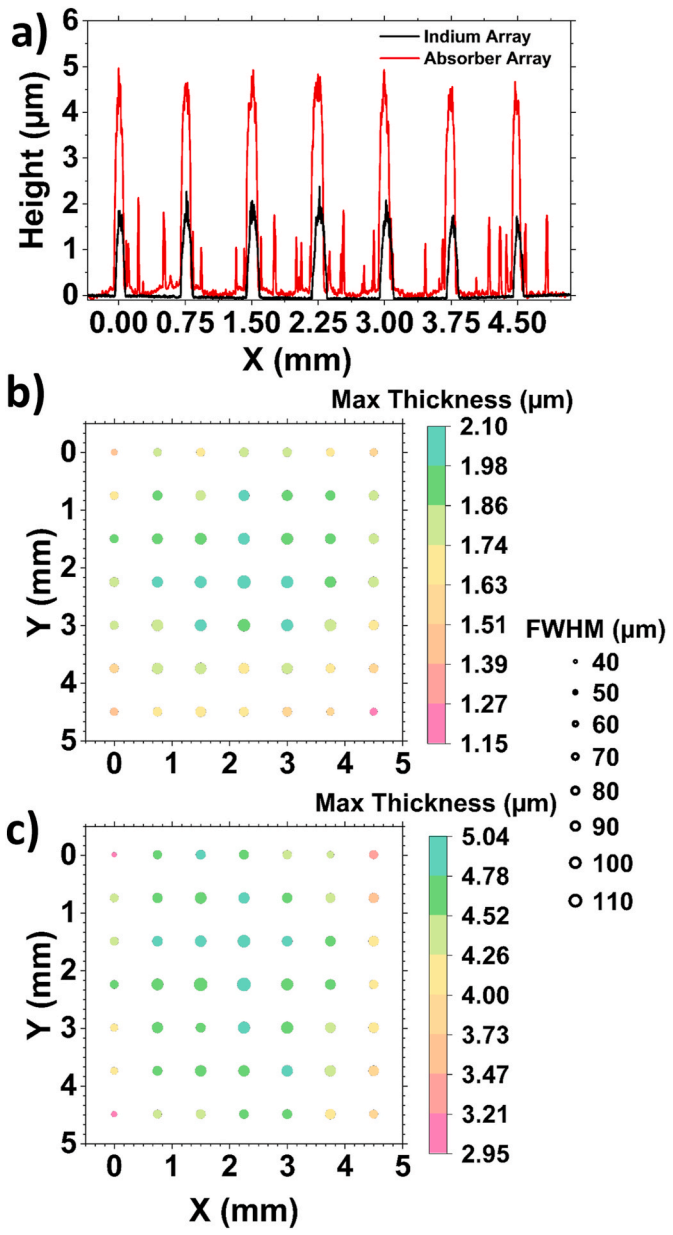

Fig. 5. Quantitative analysis of the island morphology before and after selenization using profilometry. a) A representative line scan of the 4th array line directly compares the height profiles of the initial indium islands with those of the final CISe absorbers. It is corresponding to the 4th column in the Bubble plots. b) and c) Bubble plots map the height (color) and FWHM (bubble diameter) for each island in the array for the initial indium precursor (b) and the final CISe absorber (c), respectively. Note that bubble diameters are scaled by a factor of two with respect to x and y scales for visual clarity. (For interpretation of the references to color in this figure legend, the reader is referred to the Web version of this article.)

same as for the indium islands, with the 3 × 3 array in the center being the highest. The overall largest and smallest FWHM remained at the same positions before and after the selenization. No significant gain in diameter is visible, as confirmed with an average FWHM of 79.2 ± 12.85 µm; only the variation is slightly larger. The average height is 4.4 ± 0.45 µm, and when taking the 800 nm copper layer into account the increase in height from precursor to absorber was around 1.8 µm.

For a quantitative analysis of the size distribution resulting from the intensity distribution of the DOE (compare Fig. 1 c)) used for the laser-induced growth, all SEM images from 7 different arrays were analyzed to determine the island diameters for both the initial indium arrays and the final absorber arrays. Moreover, the islands were checked for their roundness. Fig. 6 presents the analysis results, specifically focusing on the islands along the main diagonal (from position 1 at the top left to position 7 at the bottom right).

These values represent the physical diameters measured by SEM, which are distinct from the FWHM values discussed previously. The mean diameters of the indium islands (Fig. 6 a)) exhibit a strong, symmetrical spatial dependence, increasing from 44.5 µm at position 1 to a maximum of 129.4 µm at position 4, before decreasing symmetrically to 53.6 µm at position 7. (Intermediate values: 76.2 µm at position 2; 101.1 µm at position 3; 105.9 µm at position 5; 89.3 µm at position 6). This trend represents a total diameter difference of ≈164 % from the average corner to the center.

To quantify this variation, a spatial "growth factor" (the ratio of mean diameters between adjacent regions) was calculated. For the indium islands, the factor from the outer positions (1&7) to the next inner positions (2&6) is 1.69 ± 0.02. This factor then stabilizes to an average of 1.25 ± 0.05 for the subsequent steps toward the center (2&6 → 3&5 and 3&5 → 4). After selenization, the resulting absorber islands (Fig. 6 b)) show an amplified size difference at the edges, with the growth factor between positions 1&7 and 2&6 increasing to 1.83 ± 0.17. In contrast, the growth factor for the inner positions (1.27 ± 0.02) did not change significantly compared to the precursor value. Despite this edge amplification, the overall spatial distribution trend was preserved, with position 4 consistently exhibiting the maximum island diameter for both the indium precursor and the final absorber.

In the sample size of 7 arrays, the repeatability of the LA-MOCVD process appears limited, with a broad range of diameter fluctuations under nominally the same growth conditions. Nevertheless, a systematic size distribution was clearly visible for all samples. Averaged over all arrays the diameter for indium islands is 85.7 ± 30.0 µm while for the absorber it is 92.1 ± 34.7 µm, indicating no significant diameter change from processing.

The roundness of the indium islands (Fig. 6 c)) varies across the array, with an average value between 0.83 ± 0.05, indicating that the islands are nearly, but not perfectly, circular. The corner absorbers (Fig. 6 d)) at positions 1 and 7 were rounder (mean of 0.85 and 0.91, respectively) than the initial indium islands at the same positions (mean value of 0.77 and 0.85). Furthermore, the interquartile range (25% to 75%) of the roundness distribution for the central islands (Position 3,4,5) decreased, indicating less variation. For both indium and absorber arrays, the center of the array at position 4 was consistently the roundest island, with an average roundness of 0.89 and 0.94, respectively.

Comparing indium island and absorber at position 1, the mean roundness increased for the absorber while the minimum roundness has reduced further. It is likely that some absorber became loose and was cleaned from the surface. The interquartile range of the distribution narrowed for all positions except position 7. Comparing the average roundness over all arrays, indium and absorber islands differed around 0.068 with the absorber islands being rounder.

The structural characterization revealed that the indium islands grown by LA-MOCVD have the designed pitch of 750 µm. The indium islands' design size of 40 µm diameter was overshot for all islands except for the corners of the arrays. The pitch and diameter stay in a similar range when processed further to absorber islands. The uneven diameter distribution with the largest diameter in the center and decreasing diameter towards the corners of the array does not change when processed further.

3.2. *Micro-solar cell electrical characterization*

Following the geometrical and Raman analyses, the completed devices were measured under Standard Test Conditions (STC) with 1000 W/m^2 (AM1.5G spectrum) and a 25 °C micro-module temperature. For the electrical characterization, the 7 × 7 islands of one arrays were

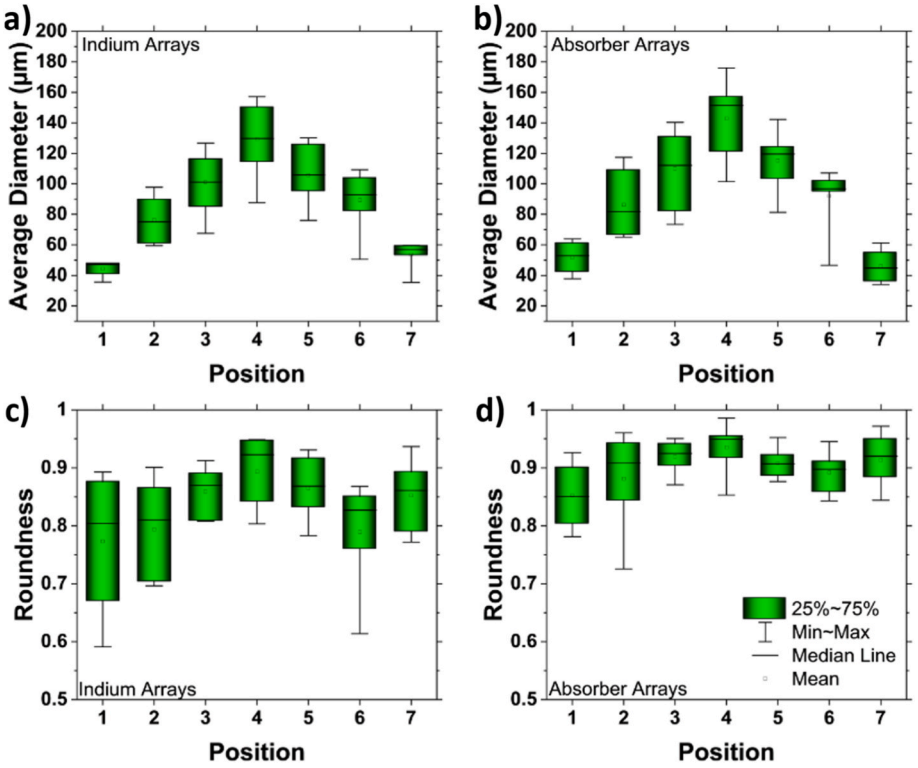

Fig. 6. *Comparison of the island diameter as a function of position along the main diagonal for a) the initial indium arrays, and b) the final CISe absorber arrays. Additional comparison of roundness for c) the initial indium arrays, and d) the final CISe absorber arrays. The central line indicates the median, the box represents the interquartile range (IQR), and the whiskers indicate the minimum and maximum values for each position, averaged over 7 arrays.*

connected in parallel to form a single micro-module. For all arrays, the total active area of the module was used to calculate the current density.

The current-voltage (IV) results of 9 arrays can be seen in Fig. 7. The mean short-circuit current density (J_{sc}) was 23.2 mA/cm^2, with values ranging from 10.0 to 33.0 mA/cm^2. The open-circuit voltage (V_{oc}) was on average 45.7 mV, with a minimum of 19.1 mV and a maximum of 101.2 mV. The average fill factor (*FF*) was at 26.6 % and varied between 24.34 and 29.23 %. The average power conversion efficiency (*PCE*) was 0.26 % under STC, with a minimum of 0.1 % and a maximum of 0.45 %. The shunt resistance (R_{sh}) ranged from 0.8 up to 25.9 Ωcm^2, while the series resistance (R_s) ranged between 0.05 and 0.58 Ωcm^2. Both resistances were extracted from a linear fit on the IV curve in the range of $V < 0$ mV for R_{sh} and V equal to V_{oc} for R_s.

The overall low performance is a result of multiple factors that could not be resolved in this sample batch. Firstly, the indium islands consist of small individual droplets, as visible in the SEM pictures, which are not

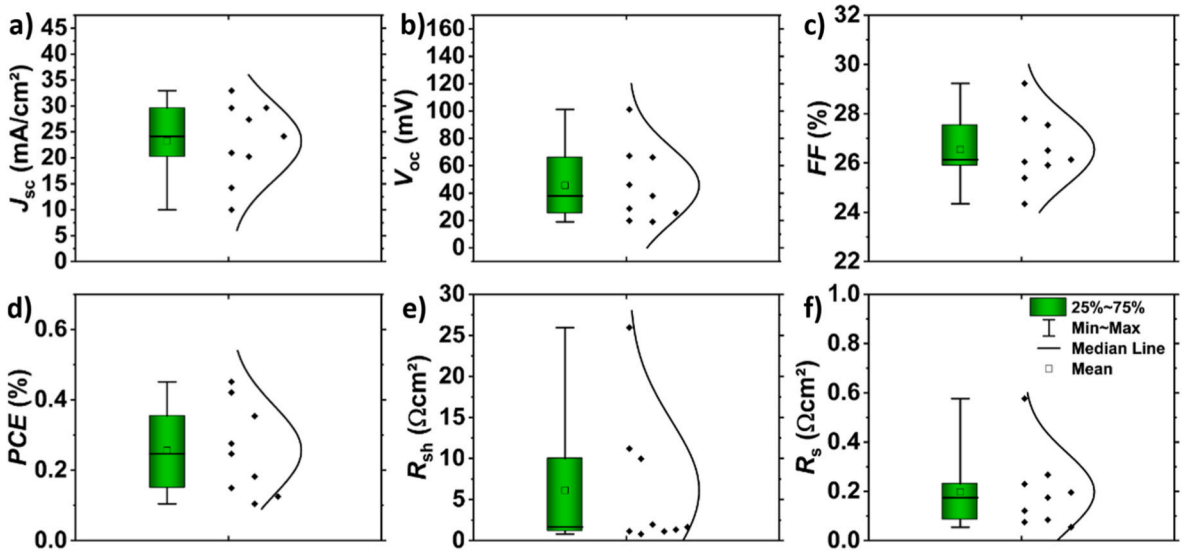

Fig. 7. Statistical distribution of photovoltaic performance parameters for 9 micro-module arrays, measured under standard test conditions (1000 W/m^2, AM1.5G, 25 °C). The box-and-whisker plots illustrate the distribution of a) short-circuit current density (J_{sc}), b) open-circuit voltage (V_{oc}), c) fill factor (*FF*), d) average power conversion efficiency (*PCE*), e) shunt resistance (R_{sh}), and f) series resistance (R_s). The central line in each box indicates the median, the box represents the interquartile range (*IQR*), and the whiskers are the minimum and maximum values across the dataset.

fully connected after selenization. The resulting poor interconnections between the individual grains and a higher density of grain boundaries may cause more shunt paths and thus recombination. This hypothesis is also supported by the low shunt resistance. Secondly, the individual openings in the photoresist insulation layer are all round. However, the islands are not perfectly round so even when using a smaller diameter for the opening a positioning error can happen leaving a shunt path to the back contact. Moreover, due to the parallel connection of 49 subcells, single bad cells can reduce the performance of the full array possibly reducing the V_{oc} and undermining the fill factor. All performance parameters, as well as the areas and the array sizes, are displayed in Table 1. For the four samples designated for concentration measurements (marked in Table 1), the measured values under 1 sun illumination in the concentrator solar simulator are shown in the parentheses below. The values measured in the 1 sun solar simulator and in the concentrator solar simulator are mismatching. Especially for array 3 and 4 the V_{oc} rise is significant. The concentrator solar simulator was calibrated with a power meter to 1000 W/m^2. Both solar simulators use a xenon lamp but only the 1 sun solar simulator uses an additional halogen lamp. The contacting was performed directly on the window layer without a grid, due to grids leading to shunting on some samples (not shown here). A different contacting method could have changed the shunt resistance. Notably, the active area of the arrays varied significantly, even with identical process parameters, ranging from 0.00232 to 0.00486 cm^2. The mean active area was 0.0039 ± 0.0009 cm^2, which highlights 23% variations in the deposition process. Even when not considering the outliers around 0.00232 cm^2 the variation would still be 12 %.

Four arrays were chosen for current-voltage tests under concentration (IV-C measurements), as also marked in Table 1: the arrays 2B, 3A and 4B with the highest $V_{oc,}$ now named Array 2, 3 and 4, and array 1A now Array 1 with efficiency in the same range as Array 2 but low V_{oc}. The results are depicted in Fig. 9. The measurements were performed with a concentrator solar simulator as specified in the experimental part. All measurements were performed under planar illumination on the full array with a manually controlled illumination time of 5-10 s per measurement and a similar waiting time after each measurement to allow for heat dissipation. Prior to the measurement, the initial concentration was calibrated to 1-sun illumination intensity using a power meter and then raised to approximately 17 suns of illumination. The measurements of Array 4 are used to calculate the concentration factors in between 1 sun and maximum concentration in the assumption of linear growth of J_{sc} with concentration. Differences in the 1 sun measurements are likely artifacts from contacting the arrays directly on the window layer. Here differences in depth of the needles could cause changes in the series and shunt resistances, influencing the measured values of J_{sc} and V_{oc}. These concentrations are used for further calculations.

The J_{sc} rises linearly with concentration, with minor kinks in the linear curve (see Fig. 8 a)). The V_{oc} curve in Fig. 8 b) demonstrates the expected logarithmic growth behavior. The kink at around 6 suns concentration is systematic and is likely an artifact of the measurement setup. The V_{oc} approaches a saturation point around 17 suns of illumination. For the fill factor in Fig. 8 c), no clear trend is visible due to the already small starting values. However, the kink at around 6 suns is also highly visible. Regarding the relative efficiency gain in Fig. 8 d), a high gain of up to 250% could be reached for the array with the lowest initial efficiency. For array 3 and 4 with the best initial efficiency, a relative gain of around 60 – 100 % is achieved. The kinks in the efficiency graph are a direct result of the systematic measurement kink in the V_{oc} and the fill factor. The shunt resistance (R_{sh}) and series resistance (R_s), shown in Fig. 8 e) and 8 f) respectively, were both observed to increase with light concentration. This trend is contrary to results reported by Lotter et al. [9], where the resistances decreased at higher concentrations. This conventional behavior is also supported by device simulations.

Thermal effects can be ruled out as the cause of the observed rise; due to active cooling, short measurement times, and equally long cooling times with good heat dissipation, the temperature can be considered constant at 25 °C. A possible cause can be photoconductivity-related effects in uncontacted but illuminated regions of the absorber. This includes not only the fully insulated grains between and around the arrays but also the parts of the absorber islands covered by photoresist. Trapped static charge can create a gating effect, passivating the shunt paths. Additionally, filled trap states can act as scattering centers for charge carriers, reducing their mobility and therefore increasing the series resistance. It also cannot be excluded that the AZ1518 photoresist itself might have a photoconductive effect on the measurement.

To investigate the dominant recombination mechanism, particularly in the device that exhibited the highest relative efficiency gain (Array 1), current-voltage versus temperature (IV-T) measurements were performed. The open-circuit voltage (V_{oc}) versus temperature curve is shown in Fig. 9.

Between 170 and 290 K, the results follow a linear trend. Notably, the V_{oc} exhibits a hysteresis, with values differing between the cooling and heating ramps; the values after cooling are lower than the values before. This is likely caused by inconsistent probe contact, as the contact needles can shift or pierce the sample during thermal cycling. Moreover, the values of V_{oc} at room temperature also differ slightly from the 1-sun solar simulator measurement, which is attributed to optical losses from the cryostat window and differences in the electrical setup.

A linear fit to the 170–290 K region, when extrapolated to 0 K, intercepts the y-axis at 154.92 mV. This value represents the activation energy (E_a) of the dominant recombination path and is significantly lower than the ~1 eV bandgap expected for CISe, indicating a strong defect level. This low activation energy leads to severe recombination and is a clear indicator of poor crystal quality, likely due to high defect densities at the grain boundaries. The slope of the fit is −0.5 mV/K. This unusually shallow slope, when compared to typical values for high-quality CIGSSe (−1.7 to −2.2 mV/K), is a direct consequence of the defect-dominated recombination and does not imply superior temperature stability. This analysis confirms that improving the absorber's

Table 1
Summary of photovoltaic performance parameters for the 7 × 7 micro-modules measured under 1-sun Standard Test Conditions (STC: 1000 W/m^2, AM1.5G, 25 °C). Key parameters presented include short-circuit current density (J_{sc}), open-circuit voltage (V_{oc}), fill factor (*FF*), power conversion efficiency (*PCE*), shunt resistance (R_{sh}), series resistance (R_s), and active area. The arrays also characterized on the concentration solar simulator (IV-C) are designated with Array 1-4 in parentheses. For these specific samples, the values measured on the IV-C at 1 sun compared to the standard IV measurement are shown in parentheses.

Name	J_{sc} (mA/cm^2)	V_{oc} (mV)	*FF* (%)	*PCE* (%)	R_{sh} (Ωcm^2)	R_s (Ωcm^2)	Array size	Active area (cm^2)
1A (Array 1)	32.959 (26.020)	28.74 (26.17)	26.05 (25.23)	0.247 (0.172)	1.15 (1.35)	0.075 (0.176)	7 × 7	0.00232
1B	29.606	19.9	25.4	0.150	0.81	0.085	7 × 7	0.00287
2A	27.391	37.98	26.51	0.276	1.97	0.121	7 × 7	0.00348
2B (Array 2)	9.997 (8.105)	66.10 (63.71)	27.54 (27.38)	0.182 (0.141)	9.97 (10.085)	0.267 (0.709)	7 × 7	0.00469
3A (Array 3)	14.230 (10.359)	101.17 (134.41)	29.23 (29.93)	0.421 (0.417)	25.94 (18.84)	0.577 (1.164)	7 × 7	0.00465
3B	20.953	19.07	26.14	0.104	1.12	0.055	7 × 7	0.00377
4A	20.239	25.42	24.34	0.125	1.35	0.174	7 × 7	0.00409
4B (Array 4)	24.154 (20.873)	67.19 (105.32)	27.80 (29.6)	0.451 (0.651)	11.20 (7.54)	0.230 (0.528)	7 × 7	0.00424
5A	29.645	46.07	25.91	0.354	1.66	0.195	7 × 7	0.00486

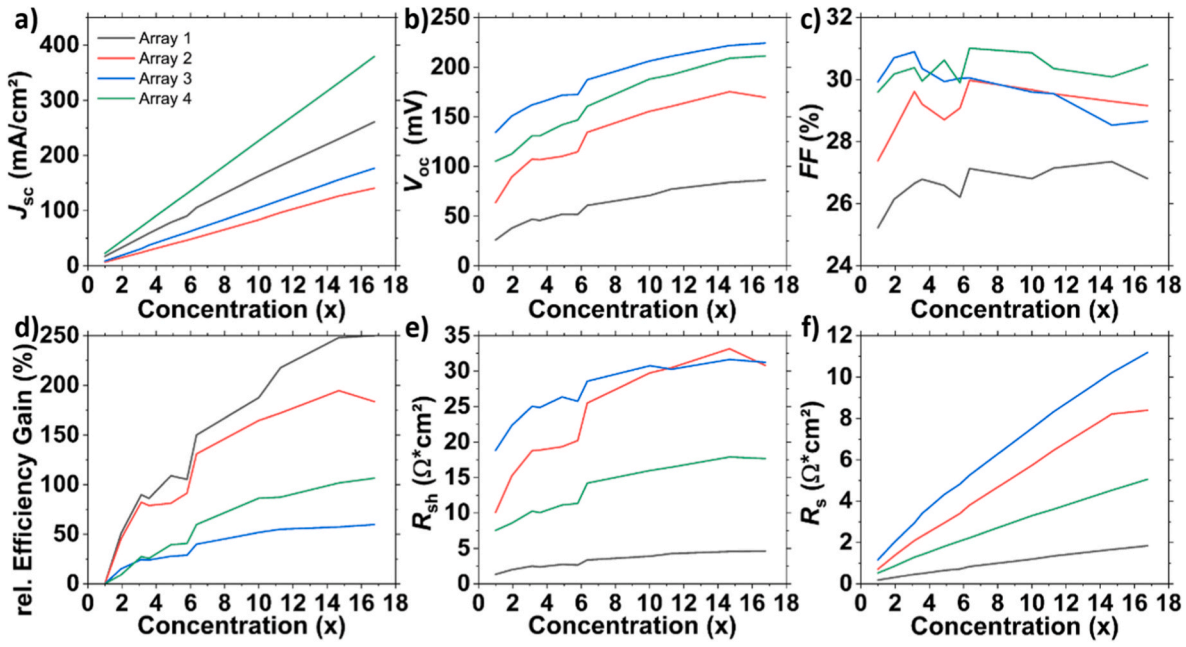

Fig. 8. Photovoltaic parameters of the four selected micro-modules as a function of light concentration, ranging from 1 to 17 suns under planar illumination. The plots show the evolution of a) the short-circuit current density (J_{sc}), b) the open-circuit voltage (V_{oc}), c) the fill factor (*FF*), d) the relative efficiency gain, e) the shunt resistance (R_{sh}), and f) the series resistance (R_s) with increasing light intensity.

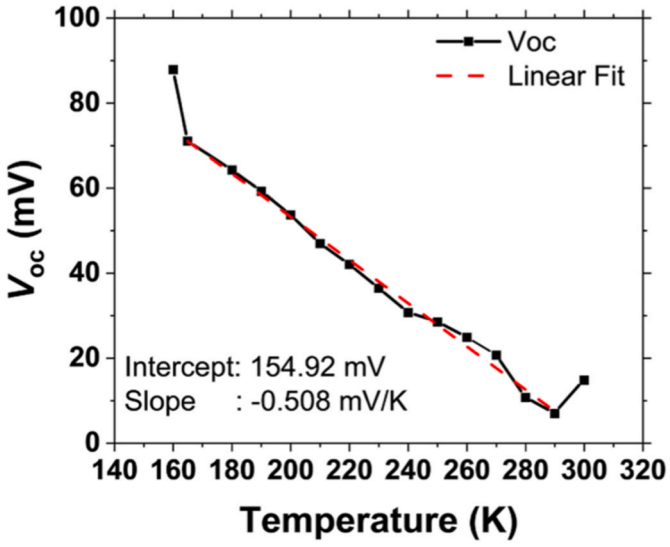

Fig. 9. Open-circuit voltage (V_{oc}) as a function of temperature for Array 1, collected from lower to higher temperatures. A linear fit to the data in the 170 K to 290 K region (red line) is shown. (For interpretation of the references to color in this figure legend, the reader is referred to the Web version of this article.)

crystal quality to reduce recombination is essential for enhancing device performance.

4. Discussion and outlook

The results of this work confirm that the LA-MOCVD technique enables the direct and simultaneous deposition of indium island arrays via localized laser heating, providing a novel route for micro-solar cell fabrication. The deposited indium was successfully processed into operational micro-solar cell modules, and an efficiency gain under concentrated light condition was observed. However, several key challenges were identified that need to be overcome for further process development.

The reproducibility of the LA-MOCVD technique falls short of establishing a reliable baseline. Further testing of growth-influencing parameters is needed to better understand the indium growth mechanism. After that, the process can be refined to enhance island quality to establish a baseline. A particular aspect requiring optimization is the morphology of the micro-droplet island. Multiple attempts of annealing under nitrogen and argon atmospheres did not show the expected outcome of remelting or coalescence of the indium into one smooth island. A possible cause for the droplets not coalescing could potentially be attributed to carbon residues on the samples resulting from the metal-organic vapor during indium deposition. To confirm the hypothesis, a future experiment involving the use of reactive hydrogen to remove carbon during deposition or annealing should be performed. After the indium island morphology is optimized, subsequent process steps can be refined to achieve a high-quality micro-concentrator solar cell array. These refinements include the adjustments of copper content, selenization conditions, spin coating, and photoresist development. Each of these optimizations extends beyond the fundamental proof-of-concept presented in this study.

The difference in diameter and height for the 7 × 7 array made the direct-write lithography for device isolation complicated. Specifically, the differences in diameter and quality of the outer array islands need adjustment for large-scale applications. Local variations in indium island diameter originate from the combination of two effects: (i) local intensity variation among the spots of the array (compare Fig. 1 c)), and (ii) a broad temperature pedestal arising from the large-scale heat dissipation constraints. The latter arises from the fact that the temperature rise from one spot does not drop down to zero at the position of the neighboring spot. This effect is most pronounced for the central spots of the array. Strategic design of the DOE can mitigate these two effects, rendering it an excellent method for parallelizing the deposition of multiple indium precursor islands.

For future commercialization the usage of a master lens array for deposition needs to be assessed as well as cost of production of lens array copies using hot embossing or other methods to easily scale production of lens arrays and reduce costs. Moreover, the spin coating is the easiest method for lab scale production, for larger modules a slot die coating or

spray coating process would need further investigation, as well as a plasma etching step to uncover the micro absorber islands.

5. Conclusion

In summary, this work has successfully demonstrated the proof-of-concept for fabricating CISe micro-solar cell modules using a mask-less LA-MOCVD technique for direct, site-selective indium deposition. This establishes a new pathway for fabricating resource-efficient micro-concentrator solar cells, characterized by excellent morphological stability throughout the fabrication process. The preliminary, unoptimized prototypes achieved a significant relative efficiency gain of 60–250% under 17 suns of light concentration.

Despite functional devices were successfully produced, notable key challenges were identified related to the intensity distribution of the DOE, the initial morphology of indium islands, and process repeatability. Addressing these challenges in terms of material quality and process control is essential. Once resolved, the LA-MOCVD method holds significant promise as a rapid and resource-efficient production technique for next-generation micro-concentrator photovoltaics.

CRediT authorship contribution statement

J. Berger: Writing – review & editing, Writing – original draft, Methodology, Investigation, Formal analysis, Data curation, Conceptualization. **S. Zahedi-Azad:** Investigation. **H. Voss:** Writing – review & editing. **O.C. Ernst:** Writing – review & editing, Investigation. **R. Hammerschmidt:** Writing – review & editing, Funding acquisition. **T. Boeck:** Writing – review & editing, Funding acquisition. **J. Martin:** Writing – review & editing. **J. Bonse:** Writing – review & editing. **J. Krüger:** Writing – review & editing, Funding acquisition. **M. Schmid:** Writing – review & editing, Supervision, Funding acquisition, Conceptualization.

Statements and declarations

The authors have no relevant financial or non-financial interests to disclose.

Funding

This research was funded by the German Federal Ministry for Economic Affairs and Climate Action (BMWK) under the contract numbers 03EE1029D (UDE), 03EE1029A (IKZ), 03 EE1029C (BAM), and 03EE1029B (Bestec).

The Raman measurements were performed on a NextGen Cluster-Tool funded by the Deutsche Forschungsgemeinschaft (DFG, German Research Foundation) - INST 20876/347-1 FUGG and are acknowledged as follows: “Gefördert durch die Deutsche Forschungsgemeinschaft (DFG) -Projektnummer INST 20876/347-1 FUGG”.

The authors acknowledge support from the Open Access Publication Fund of the University of Duisburg-Essen. Open access funding enabled and organized by Project DEAL.

Declaration of competing interest

The authors declare the following financial interests/personal relationships which may be considered as potential competing interests: All Authors report financial support was provided by Federal Ministry for Economic Affairs and Energy. Jan Berger reports article publishing charges were provided by Project DEAL. Martina Schmid reports equipment was provided by German Research Foundation. If there are other authors, they declare that they have no known competing financial interests or personal relationships that could have appeared to influence the work reported in this paper.

Acknowledgements

The authors would like to thank Prof. A. Lorke (UDE) for access to the SEM and A. Krause (UDE) for assistance with the FIB.

Appendix A. Supplementary data

Supplementary data to this article can be found online at https://doi.org/10.1016/j.solmat.2026.114284.

Data availability

Data will be made available on request.

References

[1] M. Schmid, Revisiting the definition of solar cell generations, Adv. Opt. Mater. 11 (2023) 2300697, https://doi.org/10.1002/adom.202300697.
[2] F. Ringleb, S. Andree, B. Heidmann, J. Bonse, K. Eylers, O. Ernst, T. Boeck, M. Schmid, J. Kruger, Femtosecond laser-assisted fabrication of chalcopyrite micro-concentrator photovoltaics, Beilstein J. Nanotechnol. 9 (2018) 3025–3038, https://doi.org/10.3762/bjnano.9.281.
[3] B. Heidmann, S. Andree, S. Levcenko, T. Unold, D. Abou-Ras, N. Schäfer, J. Bonse, J. Krüger, M. Schmid, Fabrication of regularly arranged chalcopyrite micro solar cells via femtosecond laser-induced forward transfer for concentrator application, ACS Appl. Energy Mater. 1 (2018) 27, https://doi.org/10.1021/acsaem.7b00028.
[4] B. Heidmann, F. Ringleb, K. Eylers, S. Levcenco, J. Bonse, S. Andree, J. Krüger, T. Unold, T. Boeck, M.C. Lux-Steiner, M. Schmid, Local growth of $CuInSe_2$ micro solar cells for concentrator application, Mater. Today Energy 6 (2017) 238–247, https://doi.org/10.1016/j.mtener.2017.10.010.
[5] D. Siopa, K. El Hajraoui, S. Tombolato, F. Babbe, A. Lomuscio, M.H. Wolter, P. Anacleto, K. Abderrafi, F.L. Deepak, S. Sadewasser, P.J. Dale, Micro-sized thin-film solar cells via area-selective electrochemical deposition for concentrator photovoltaics application, Sci. Rep. 10 (2020) 14763, https://doi.org/10.1038/s41598-020-71717-0.
[6] R.G. Poeira, A. Pérez-Rodríguez, A.J.C.M. Prot, M. Alves, P.J. Dale, S. Sadewasser, Direct fabrication of arrays of $Cu(In,Ga)Se_2$ micro solar cells by sputtering for micro-concentrator photovoltaics, Mater. Des. 225 (2023) 111597, https://doi.org/10.1016/j.matdes.2023.111597.
[7] D. Sancho-Martínez, M. Schmid, Thermal management approaches of $Cu(In_x, Ga_{1-x})Se_2$ micro-solar cells, J. Phys. Appl. Phys. 50 (2017), https://doi.org/10.1088/1361-6463/aa8ac5.
[8] S. Sadewasser, P.M.P. Salomé, H. Rodriguez-Alvarez, Materials efficient deposition and heat management of $CuInSe_2$ micro-concentrator solar cells, Sol. Energy Mater. Sol. Cell. 159 (2017) 496–502, https://doi.org/10.1016/j.solmat.2016.09.041.
[9] E. Lotter, P. Jackson, S. Paetel, W. Wischmann, Identification of loss mechanisms in CIGS micro-cells for concentrator applications, in: 32nd EU-PVSEC, 2016. Munich.
[10] B. Reinhold, M. Schmid, D. Greiner, M. Schüle, D. Kieven, A. Ennaoui, M.C. Lux-Steiner, Monolithically interconnected lamellar $Cu(In,Ga)Se_2$ micro solar cells under full white light concentration, Prog. Photovoltaics Res. Appl. 23 (2015) 1929–1939, https://doi.org/10.1002/pip.2611.
[11] M. Paire, L. Lombez, F.d.r. Donsanti, M. Jubault, S.p. Collin, J.-L. Pelouard, J.-F. o. Guillemoles, D. Lincot, $Cu(In, Ga)Se_2$ microcells: high efficiency and low material consumption, J. Renew. Sustain. Energy 5 (2013) 011202, https://doi.org/10.1063/1.4791778.
[12] M. Schmid, B. Heidmann, F. Ringleb, K. Eylers, O. Ernst, S. Andree, J. Bonse, T. Boeck, J. Krüger, Locally grown Cu(In,Ga)Se2 micro islands for concentrator solar cells, in: Proc.Spie., 2018.
[13] M. Schmid, E. Lotter, X. Lin, L. Wang, R. Klenk, K. Eylers, F. Ringleb, T. Boeck, B. Heidmann, G. Nenna, F. Loffredo, F. Villani, T. Köhler, D. Sancho-Martinez, T. Raadik, J. Krustok, M. Grossberg, M.C. Lux-Steiner, Micro concentrator concept for cost reduction and efficiency enhancement of thin-film chalcopyrite photovoltaics: results from eu joint research program CHEETAH, in: 33rd EU-PVSEC, 2017, pp. 1077–1080. Amsterdam.
[14] H. Voss, S. Zahedi-Azad, O.C. Ernst, J. Lucaßen, G. Mann, J. Bonse, T. Boeck, J. Martin, M. Schmid, J. Krüger, Chemical vapor deposition of indium precursors for solar micro-absorbers using continuous laser radiation, Appl. Phys. A 131 (2025) 781, https://doi.org/10.1007/s00339-025-08895-z.
[15] C.A. Larsen, G.B. Stringfellow, Decomposition kinetics of OMVPE precursors, J. Cryst. Growth 75 (1986) 247–254, https://doi.org/10.1016/0022-0248(86)90034-5.
[16] K. Eylers, F. Ringleb, B. Heidmann, S. Levcenco, T. Unold, H.W. Klemm, G. Peschel, A. Fuhrich, T. Teubner, T. Schmidt, M. Schmid, T. Boeck, In-Ga precursor islands for $Cu(In,Ga)Se_2$ micro-concentrator solar cells, in: Proceedings of the IEEE 44th Photovoltaic Specialist Conference, IEEE, Washington DC, 2017.
[17] E.P. Zaretskaya, V.F. Gremenok, V. Riede, W. Schmitz, K. Bente, V.B. Zalesski, O. V. Ermakov, Raman spectroscopy of CuInSe2 thin films prepared by selenization, J. Phys. Chem. Solid. 64 (2003) 1989–1993, https://doi.org/10.1016/S0022-3697(03)00216-6.
[18] V. Singh, V.G. Sathe, S. Rath, Raman spectroscopic study of the layer-dependent Davydov splitting and thermal conductivity of chemically vapor deposited two-

dimensional MoSe2, Appl. Phys. Lett. 122 (2023), https://doi.org/10.1063/5.0123628.
[19] D. Nam, J.-U. Lee, H. Cheong, Excitation energy dependent raman spectrum of MoSe2, Sci. Rep. 5 (2015) 17113, https://doi.org/10.1038/srep17113.
[20] M. Gilić, M. Petrović, R. Kostić, D. Stojanović, T. Barudžija, M. Mitrić, N. Romčević, U. Ralević, J. Trajić, M. Romčević, I.S. Yahia, Structural and optical properties of $CuSe_2$ nanocrystals formed in thin solid Cu–Se film, Infrared Phys. Technol. 76 (2016) 276–284, https://doi.org/10.1016/j.infrared.2016.03.008.